optica

Perfect single-sided radiation and absorption without mirrors

HENGYUN ZHOU,[1] BO ZHEN,[2,3,*] CHIA WEI HSU,[4] OWEN D. MILLER,[5] STEVEN G. JOHNSON,[5] JOHN D. JOANNOPOULOS,[1,2] AND MARIN SOLJAČIĆ[1,2]

[1]Department of Physics, Massachusetts Institute of Technology, 77 Massachusetts Avenue, Cambridge, Massachusetts 02139, USA
[2]Research Lab of Electronics, Massachusetts Institute of Technology, 77 Massachusetts Avenue, Cambridge, Massachusetts 02139, USA
[3]Physics Department and Solid State Institute, Technion, Haifa 32000, Israel
[4]Department of Applied Physics, Yale University, New Haven, Connecticut 06520, USA
[5]Department of Mathematics, Massachusetts Institute of Technology, 77 Massachusetts Avenue, Cambridge, Massachusetts 02139, USA
*Corresponding author: bozhen@mit.edu

Received 15 July 2016; revised 23 August 2016; accepted 23 August 2016 (Doc. ID 270651); published 21 September 2016

Highly directional radiation from photonic structures is important for many applications, including high-power photonic crystal surface-emitting lasers, grating couplers, and light detection and ranging devices. However, previous dielectric, few-layer designs only achieved moderate asymmetry ratios, and a fundamental understanding of bounds on asymmetric radiation from arbitrary structures is still lacking. Here, we show that breaking the 180° rotational symmetry of the structure is crucial for achieving highly asymmetric radiation. We develop a general temporal coupled-mode theory formalism to derive bounds on the asymmetric decay rates to the top and bottom of a photonic crystal slab for a resonance with arbitrary in-plane wavevector. Guided by this formalism, we show that infinite asymmetry is still achievable even without the need for back-reflection mirrors, and we provide numerical examples of designs that achieve asymmetry ratios exceeding 10^4. The emission direction can also be rapidly switched from top to bottom by tuning the wavevector or frequency. Furthermore, we show that with the addition of weak material absorption loss, such structures can be used to achieve perfect absorption with single-sided illumination, even for single-pass material absorption rates less than 0.5% and without back-reflection mirrors. Our work provides new design principles for achieving highly directional radiation and perfect absorption in photonics.

OCIS codes: (230.1950) Diffraction gratings; (230.5298) Photonic crystals.

http://dx.doi.org/10.1364/OPTICA.3.001079

1. INTRODUCTION

Due to their ease of fabrication and integration, as well as their large area and high-quality factor of resonances [1], photonic crystal slabs with one- or two-dimensional periodicity [2–4] have been widely used in many applications, such as filters [5], lasers [6], and sensors [7]. For more efficient utilization of light, it is often desirable to achieve highly directional out-of-plane coupling of light from photonic crystal slabs, in which light predominantly radiates to only one side of the slab. This would eliminate the need for a back-reflection mirror in high-power photonic crystal surface-emitting lasers (PCSELs) [6], where fabrication uncertainties in the laser wavelength and mirror-cavity distance currently make reliably achieving high slope efficiency difficult. This could also lead to increased efficiency of grating couplers for silicon photonics and light detection and ranging (LIDAR) devices. Previous designs of grating couplers have achieved a top-down asymmetry ratio (defined as the ratio of power going to the top and to the bottom) of up to 50 : 1 [8–11], but they typically make use of a substrate reflector or involve multiple layers and grooves [12], which complicates fabrication and could be difficult to scale to larger areas if desired. Asymmetric out-of-plane emission from photonic crystal defect cavities of 4 : 1 has also been demonstrated [13], but all these works were guided primarily by numerical optimization. It is thus important to gain an understanding of the fundamental bounds on asymmetric radiation and use such bounds as a guide to design stronger asymmetries.

Closely related to highly directional radiation is achieving perfect absorption of fields incident from a single side of a weakly absorbing photonic structure. This can be viewed as the time-reversal partner of the single-sided radiation emission process. An increased absorption efficiency could be important for improving the performance of many devices, including modulators [14], photodetectors [15], solar cells [16,17]. However, the single-pass absorption of a thin absorbing layer in air is at most 50% [18,19]. By combining electric and magnetic responses or utilizing material anisotropy, it is possible to design metamaterial perfect absorbers with near-unity absorptance [19–22], but such designs can be difficult to implement at optical frequencies. Recent work achieving perfect absorption in photonic crystal structures has either employed illumination from both sides and used the interference between the beams—analogous to a time-reversed laser—to achieve coherent perfect absorption [23–25] or employed a back-reflection mirror and critical coupling to resonances to approach perfect absorption [26–32]. Alternatively, specific surface textures can be designed to enhance light trapping and subsequent absorption [16,33,34], but a back-reflection mirror is still required to keep the photons inside the absorbing layer. In general, however, two-sided illumination can often be challenging to implement in realistic systems, while backing mirrors are often either lossy (e.g., metallic mirrors) or require additional fabrication efforts (e.g., distributed Bragg reflectors). Therefore, the possibility of achieving perfect absorption of fields incident from a single side, without the aid of backing mirrors, is highly attractive and could open up many engineering possibilities. One recent approach to achieving this is to utilize accidental degeneracies of critically coupled modes with opposite symmetries [35], but such an approach requires aligning the frequencies and quality factors of multiple resonances. Here, we first design structures with highly directional radiation and then consider the time-reversal scenario at critical coupling to realize devices with high absorption efficiency. Moreover, away from the strongly absorbing resonance frequency, light can be mostly transmitted through the designed devices, which could have important applications in multi-junction solar cells.

Previous work [36] has used a temporal coupled-mode theory (TCMT) formalism [37,38] with a single resonance and two coupling ports (one on each side of the slab) to examine bounds of asymmetric radiation from photonic crystal slabs. There, they reached the conclusion that the asymmetry ratio is bounded by $(1+r)/(1-r)$, where r is the background amplitude reflection coefficient. For index contrasts found in realistic materials and at optical frequencies, this bound limits the proportion of radiation going to one side of the photonic crystal slab to around 90%, even for the high index contrast between silicon and air. For a smaller index contrast, this will be even more significantly different from perfect directional radiation. We find, however, that in more general scenarios, the bounds in Ref. [36] can be greatly surpassed.

In a periodic photonic structure, the natural choice of mode basis is the momentum-conserving Bloch-wave basis [39]. As shown in Fig. 1(a), for general incident directions (nonzero in-plane momentum $\vec{k}_{\parallel}$) in asymmetric structures, the time-reversal operation relates the resonance at $\vec{k}_{\parallel}$ to the resonance at $-\vec{k}_{\parallel}$, suggesting that a two-resonance, four-port model is required to impose time-reversal constraints in the more general case. Moreover, reciprocity automatically ensures that the two resonances share identical frequencies, eliminating the need for exquisite degenerate-frequency alignment to achieve multi-resonant responses. Only when the system under consideration possesses certain symmetries—either in the structure [40] (C_2^z, i.e., 180° rotation around the out-of-plane axis) or in the incident field (normal incidence)—can we use the simplified model [36] with only a single independent port on each side of the slab.

In this paper, we show that the general two-resonance, four-port TCMT formalism widely applicable to periodic structures with arbitrary geometry or in-plane momentum enables bounds with significantly higher (sometimes even infinitely high) radiation asymmetry for realistic materials when the C_2^z symmetry of the structure is broken. As an example, we apply this formalism to inversion-symmetric (P-symmetric) structures without C_2^z symmetry. Through numerical examples, we show that a top-down asymmetry

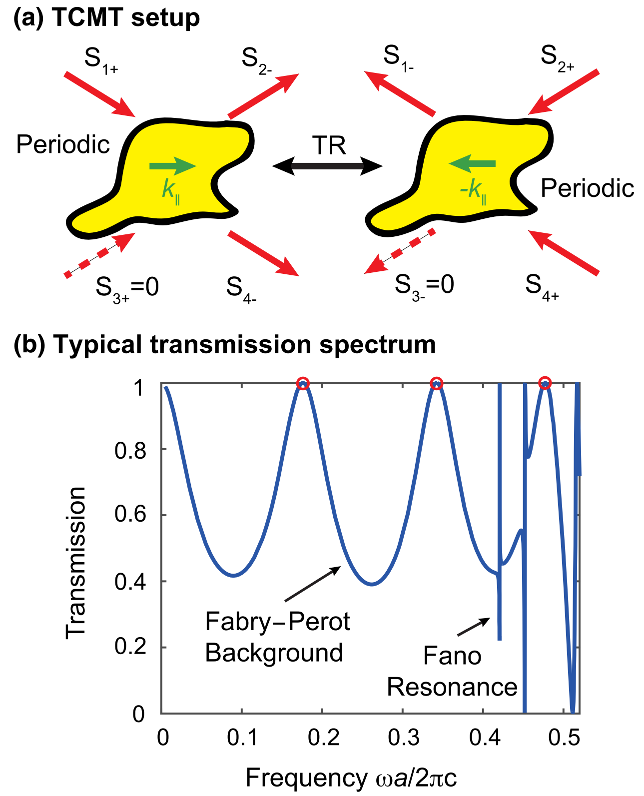

Fig. 1. Temporal coupled-mode theory setup and transmission spectrum. (a) Schematic of our TCMT setup with four ports and two resonances related by the time-reversal operation. This general setup is valid for structures with arbitrary shapes and incident angles as long as the assumption of four ports and two resonances is correct. (b) Typical transmission spectrum of an inversion-symmetric, C_2^z-symmetry-broken structure, with the Fano resonances exhibiting full transmission at certain frequencies as predicted by our TCMT formalism. Strong asymmetry is achieved when the Fano resonance is aligned with the frequencies where the background reaches full transmission (red circles).

ratio exceeding 10^4 can be achieved by tuning the resonance frequency to coincide with the perfectly transmitting frequency on the Fabry–Perot background. The emission direction can also be rapidly switched from top to bottom by tuning the $\vec{k}_{\parallel}$ vector or frequency. These results provide important design principles for PCSELs, grating couplers, LIDARs, and many other applications that could benefit from directional emission and rapid tuning. In addition, we derive analytical expressions for the transmission spectrum and discuss features such as full transmission or reflection. We then show that such highly asymmetric coupling to the two sides of the photonic crystal slab can also be employed to achieve perfect absorption of light incident from one side of the slab, without the need for back-reflection mirrors as in previous designs.

2. TEMPORAL COUPLED-MODE THEORY FORMALISM

We start by considering arbitrary photonic crystal slab structures embedded in a uniform medium (identical substrate and superstrate). We assume weak coupling, linearity, energy conservation, and time-reversal symmetry in the system, and we consider frequencies below the diffraction limit so that higher-order diffractions are not present. A plane wave with in-plane momentum

$\vec{k}_\parallel = (k_x, k_y)$ incident from the top [port 1, see Fig. 1(a)] will only couple to resonances and outgoing waves with the same $\vec{k}_\parallel$ (conservation of Bloch momentum). We shall consider the typical case where there is a single resonance at $\vec{k}_\parallel$ near the frequencies of interest, with the transmission spectrum consisting of a Fabry–Perot background and sharp resonant features, as in Fig. 1(b). To describe time-reversal symmetry constraints for general geometries and incident angles, we need to include the resonance at $-\vec{k}_\parallel$ in our description as well, resulting in a two-resonance, four-port model. Although conservation of Bloch momentum means that each input port only excites either the $\vec{k}_\parallel$ or $-\vec{k}_\parallel$ resonance, the two resonances still influence one another indirectly via the time-reversal symmetry constraints on the coupling matrices between resonances and ports [K and D in Eq. (1)], as described below. Writing down expressions consistent with momentum conservation and time-reversal symmetry, we obtain the TCMT equations

$$\frac{d\mathbf{A}}{dt} = \left(j\omega - \frac{1}{\tau} - \frac{1}{\tau_{nr}}\right)\mathbf{A} + K^{\mathrm{T}}|s_+\rangle, \qquad |s_-\rangle = C|s_+\rangle + D\mathbf{A}, \tag{1}$$

$$C = e^{j\phi}\begin{pmatrix} 0 & r & 0 & jt \\ r & 0 & jt & 0 \\ 0 & jt & 0 & r \\ jt & 0 & r & 0 \end{pmatrix}, \qquad D = K\sigma_x = \begin{pmatrix} 0 & d_1 \\ d_2 & 0 \\ 0 & d_3 \\ d_4 & 0 \end{pmatrix}, \tag{2}$$

where $\mathbf{A} = (A_1, A_2)^T$ are the amplitudes of the two resonances (at $\vec{k}_\parallel$ and $-\vec{k}_\parallel$, respectively), ω is the resonance frequency shared by both resonances, τ is the radiative e^{-1}-decay lifetime (ω, τ are identical for the two resonances due to reciprocity), τ_{nr} is the e^{-1}-decay lifetime for nonradiative processes such as absorption, and $|s_+\rangle = (s_{1+}, s_{2+}, s_{3+}, s_{4+})^T$, $|s_-\rangle = (s_{1-}, s_{2-}, s_{3-}, s_{4-})^T$ are the amplitudes of the incoming and outgoing waves. C is the scattering matrix for the direct (nonresonant) transmission and reflection through the slab (namely, the Fabry–Perot background). Energy conservation and reciprocity constrain C to be unitary and symmetric. For identical substrates and superstrates, C takes the form in Eq. (2), where t and r are real numbers satisfying $r^2 + t^2 = 1$ that characterize the Fabry–Perot background, and the phase ϕ depends on the choice of reference plane position. K and D are the coupling matrices in and out of the resonances. Time reversal flips the two resonances, so instead of the usual relation $D = K$ [37], here we have $D = K\sigma_x$, where σ_x is the 2×2 X-Pauli matrix acting to flip the resonances. We note that an alternative (and equivalent) formalism is to adopt a basis in which the underlying modes are time-reversal invariant (for which the standard multimode treatment [37] is adequate), by superimposing the resonance at $\vec{k}_\parallel$ with its time-reversal partner at $-\vec{k}_\parallel$. This is to be contrasted with a basis change for ports, as discussed in Ref. [41]. Detailed derivations of this and the following expressions are given in Supplement 1.

Energy conservation and time-reversal symmetry impose constraints on the coefficients. Energy conservation requires

$$|d_2|^2 + |d_4|^2 = |d_1|^2 + |d_3|^2 = \frac{2}{\tau}, \tag{3}$$

while time-reversal symmetry gives the constraint $D = K\sigma_x$ and the two independent equations

$$e^{j\phi}(rd_2^* + jtd_4^*) + d_1 = 0, \tag{4}$$

$$e^{j\phi}(jtd_2^* + rd_4^*) + d_3 = 0. \tag{5}$$

In the following, we shall fix the phase ϕ to be 0 by appropriately choosing the location of our reference plane. Equations (3)–(5) impose constraints on the values and phases of the couplings and hence constrain the transmission spectrum and set bounds on the asymmetric coupling ratios.

From the preceding equations, we can derive an expression for the transmission spectrum [36,38] that only depends on the frequencies and decay rates of the resonances and the transmission and reflection coefficients of the direct Fabry–Perot pathway.

The full scattering matrix, including the direct pathway and resonance pathway [37], is given by Eq. (S25) in Supplement 1. The power reflection and transmission coefficient for a wave incident from port 1 correspond to the amplitude squared of the (1, 2), (1, 4) element of the scattering matrix, given by

$$R = |S_{12}|^2 = \left| e^{j\phi}r + \frac{d_1 d_2}{j(\omega - \omega_0) + \frac{1}{\tau} + \frac{1}{\tau_{nr}}} \right|^2, \tag{6}$$

$$T = |S_{14}|^2 = \left| e^{j\phi}jt + \frac{d_1 d_4}{j(\omega - \omega_0) + \frac{1}{\tau} + \frac{1}{\tau_{nr}}} \right|^2 \tag{7}$$

and the power reflection coefficient can be rewritten in the lossless limit $\tau_{nr} \to \infty$ as

$$R = \frac{\left[r(\omega - \omega_0) \pm \sqrt{\frac{4}{\tau_1\tau_2} - \frac{r^2}{\tau^2} - \frac{2}{\tau\sigma} - \frac{1}{\sigma^2 r^2}} \right]^2 + \left(\frac{1}{\sigma r}\right)^2}{(\omega - \omega_0)^2 + \frac{1}{\tau^2}}, \tag{8}$$

where we have written $\tau_i = 2/|d_i|^2$, $1/\sigma = 1/\tau_1 - 1/\tau_4$ to simplify the expression.

This expression provides general conditions for reaching full transmission or reflection with the Fano resonance. As shown in Supplement 1, full transmission $R = 0$ can only occur when the coupling rates satisfy $\tau_1 = \tau_4$, $\tau_2 = \tau_3$ (P-symmetric coupling), consistent with the transmission spectrum shown in Fig. 1(b). Full reflection $R = 1$ can only occur when the coupling rates satisfy $\tau_1 = \tau_2, \tau_3 = \tau_4$ (C_2^z symmetric coupling), consistent with the results in Ref. [36]. Note that for structures that do not have P or C_2^z symmetry, it is still possible for the coupling rates for resonances to be P or C_2^z symmetric, leading to full transmission/reflection features in the frequency spectrum (see for example Supplement 1, Fig. S1).

3. GENERAL BOUNDS ON ASYMMETRIC COUPLING RATES

We now derive bounds on the achievable asymmetry of coupling to the top and bottom based on Eqs. (4) and (5) derived from time-reversal symmetry. Denote $|d_4/d_2| = a_r$, $|d_3/d_1| = a_\ell$, and define the asymmetric coupling ratios on the right ($\vec{k}_\parallel$) and left ($-\vec{k}_\parallel$) directions of the resonator as a_r^2 and a_ℓ^2 (the ratio of the power going to bottom and top). By taking the ratio of Eqs. (4) and (5), we find

$$a_\ell^2 = \left| \frac{jt + ra_r e^{j\theta}}{r + jta_r e^{j\theta}} \right|^2 = \frac{t^2 + r^2 a_r^2 + 2tra_r \sin\theta}{r^2 + t^2 a_r^2 - 2tra_r \sin\theta}, \tag{9}$$

where $\theta = \arg(d_2) - \arg(d_4)$ characterizes the phase difference between d_2 and d_4. This gives the bound

$$\left|\frac{t - ra_r}{r + ta_r}\right| \leq a_\ell \leq \left|\frac{t + ra_r}{r - ta_r}\right|. \quad (10)$$

Therefore, the amount of achievable asymmetry to top and bottom on the left is bounded by that on the right, and vice versa. Note that in general, the phase here can be tuned through a 2π cycle, so the bounds—even up to infinitely high asymmetry ratios—should be saturable for the appropriate parameter choices. The coefficients that enter the bounds are the transmission/reflection coefficients (t, r) of the direct process (Fabry–Perot background), as opposed to the total transmission/reflection including the resonant pathway.

If the structure has C_2^z symmetry, the two channels on the top and bottom will be constrained to have the same coupling rates, so $d_1 = d_2$, $d_3 = d_4$, $a_\ell = a_r$. Plugging this into Eq. (10), we find the same bound as in Ref. [36]: $\frac{1-r}{1+r} \leq a_\ell^2 = a_r^2 \leq \frac{1+r}{1-r}$, which shows the consistency of our approach. In typical photonic crystal systems at optical frequencies, the index contrast between the slab and the background medium is limited to around 3, which constrains the interface reflection coefficient to be less than 0.5 for most incident angles. This results in the Fabry–Perot direct pathway reflection coefficient $r = \sqrt{1 - t^2}$ being considerably smaller than 1, so strong asymmetry in the decay rates is difficult to achieve for C_2^z-symmetric structures without the use of an additional back-reflecting mirror.

The general bound Eq. (10) suggests, however, that much stronger asymmetry can be achieved if we break the C_2^z symmetry of the system. A simple example is when the structure possesses inversion symmetry P but breaks the C_2^z symmetry, as shown in Fig. 2(a). In this case, the decay rates must satisfy $d_1 = d_4$, $d_2 = d_3$, $a_\ell = 1/a_r$, and Eq. (10) becomes

$$\frac{1 - t}{1 + t} \leq a_\ell^2 = \frac{1}{a_r^2} \leq \frac{1 + t}{1 - t}. \quad (11)$$

For any index contrast, due to the up–down symmetry of the background material, the Fabry–Perot background will always have frequencies with full transmission, as exemplified by the red circles in Fig. 1(b). Therefore, by tuning the resonance frequency to such points, the lower and upper bounds of Eq. (11) approach 0 and $+\infty$. Moreover, the bound can be saturated for appropriate choices of structural parameters and wavevectors, yielding arbitrarily high asymmetric decay rates of the photonic structure in the top and bottom directions. We note that similar design principles of breaking the C_2^z symmetry to achieve higher radiation asymmetry have also been realized in Ref. [42] using the different design intuition of destructive interference.

To verify these analytical results, we perform numerical simulations using the finite-difference time-domain (FDTD) method [43] with a freely available software package [44]. We extract the coupling rate to the top or bottom by monitoring the field amplitude at reference planes placed in the far field and determine the Fabry–Perot background transmissivity from plane-wave excitation calculations. The results are given in Fig. 2(b), where each data point in the figure (blue cross) represents the maximal asymmetric coupling ratio searching over all k points in the Brillouin zone, for P-symmetric structural parameter choices [Fig. 2(a)] with $h = 1.5a$, $w = 0.45a$, $n_0 = 1.45$, and varying n_d and d (see Supplement 1 for more details). We can see that all data points obey the bound Eq. (11) derived above (red solid lines). Moreover, this bound can be saturated for each value of the background transmission coefficient by appropriate optimization of the structural parameters and in-plane momentum. The blue crosses that do not saturate the bound are structures with very little perturbation from C_2^z symmetry due to the choice of structural parameters.

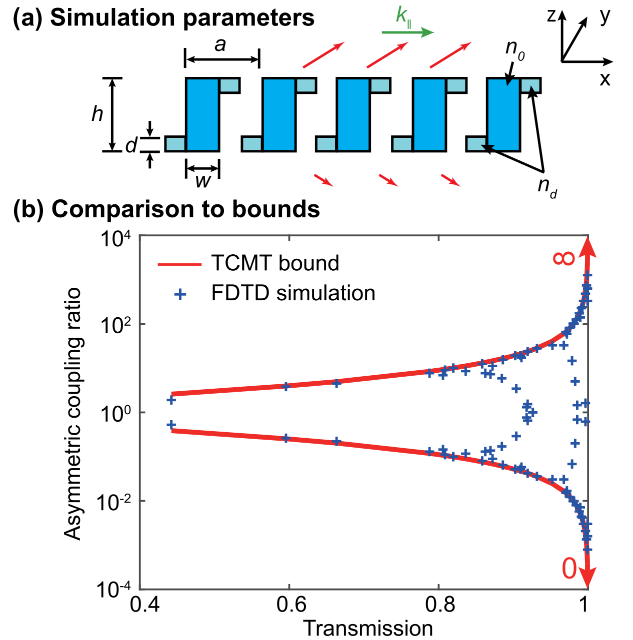

Fig. 2. Simulated structures and verification of TCMT bounds. (a) The P-symmetric structure we use in our numerical examples and its structural parameters. a: periodicity of photonic crystal, h: height of central slab, w: width of central slab, n_0: refractive index of central slab, d: height of additional pieces on the sides (the width of the additional pieces is $(a - w)/2$), n_d: refractive index of additional pieces on the sides; (b) numerical verification of TCMT bounds on asymmetric radiation for P-symmetric structures. Red lines indicate the bound from Eq. (11). Each blue cross indicates simulation results of the asymmetry for a given structure, optimized over in-plane momentum. The transmissivity t is fitted from the Fabry–Perot background, and the asymmetric coupling ratio is calculated from the Poynting flux in the top and bottom directions.

4. EXAMPLES OF HIGHLY ASYMMETRIC RADIATION

In this section, we provide numerical examples of strong asymmetry that highlight two features of the extreme data points in Fig. 2 that are not obvious from the preceding data: it is possible to achieve high asymmetry even at the point of highest quality factor, and it is possible to achieve rapid tuning of the direction of asymmetry by slightly changing the frequency. As the form $(1 + t)/(1 - t)$ of the bound (for P-symmetric structures) suggests, strong asymmetry can be achieved when the resonance frequency coincides with locations of large transmissivity on the Fabry–Perot background for any refraction index contrast.

We optimize over the structural parameters shown in Fig. 2(a) to find examples of high asymmetry in coupling to the top and bottom. This example consists of the second transverse electric (TE) polarization band (nonzero E_z, E_x, H_y, classified by mirror symmetry with respect to the $x - z$ plane) of a 1D photonic crystal with structural parameters $h = 1.5a$, $w = 0.45a$, $n_0 = n_d = 1.45$, $d = 0.3a$, as defined in Fig. 2(a). See Supplement 1 for a plot of the band structure. The resulting asymmetry ratio and quality factor (Q) as a function of the in-plane k_x, along with the radiation field distribution at maximal asymmetry, are shown in Fig. 3(a). The resonance frequency lies very close to a point of full transmission on the Fabry–Perot background and exhibits an asymmetry exceeding 10^4 at the $\vec{k}_\parallel$ point of largest asymmetry as well as an asymmetry over 300 at the point of highest quality factor. It may therefore be possible to produce a laser that preferentially emits to the top or bottom using the principles discussed above.

Another application of our results is the rapid steering of the direction of light emission by slight tuning of the frequency, which could be useful for LIDARs [45] or antennas. We design such a structure by perturbing a bound state in the continuum (BIC) [40,46–48]. BICs are localized solutions embedded in the radiation continuum, where, due to the destructive interference of the amplitude for the decay between outgoing wave channels, the quality factor of a resonance above the light line approaches infinity. In previous works [40,46,47], the photonic structures were chosen to have both P and C_2^z symmetries. With a perturbation that breaks C_2^z but preserves P, the peak quality factor will be finite but still very high [47]. We expect that this symmetry breaking will also split the momenta where radiation toward the top and toward the bottom vanish, thereby creating strong asymmetry in the two directions, with the extrema separated only by a small $\vec{k}_\parallel$.

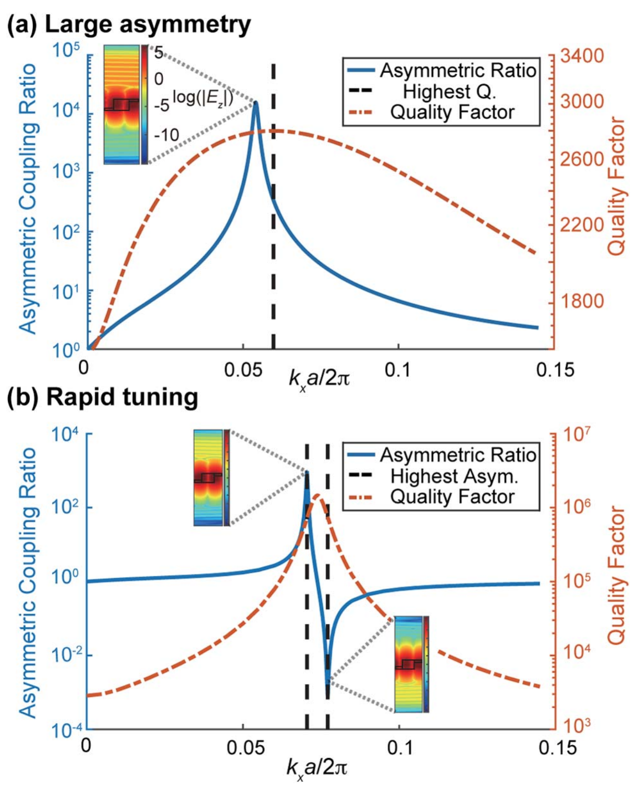

Fig. 3. Examples of highly asymmetric radiation. (a) Plot of the asymmetry ratio and quality factor as a function of k_x, along the $k_y = 0$ axis in momentum space. Strong asymmetric radiation occurs over a range of momenta, including the point of highest quality factor. Inset: log scale plot of the z-component of the electric field amplitude at the highest asymmetry point. (b) Similar plot for a different set of parameters, showing rapid switching of asymmetric direction by tuning the frequency or in-plane momentum.

We choose $h = 1.5a$, $w = 0.45a$, $n_0 = 1.45$, $d = 0.1a$, and $n_d = 1.1$, again examining the second TE band. The resulting asymmetry ratio and frequency are shown in Fig. 3(b). The asymmetric coupling flips from mostly radiating to the top to mostly radiating to the bottom (by a factor of 10^4) when k_x is changed by as small as $0.05 \times 2\pi c/a$ or equivalently, when the frequency is changed by $3 \times 10^{-4} \times 2\pi c/a$. The radiative quality factors of these resonances are on the order of 10^6, so these two bands will be well separated in emission. One can thereby envision rapid tuning of the emission direction by changing the frequency of radiation slightly. Moreover, the high Q of these resonances will enable long propagation lengths for collimated emission from large areas, which is important for LIDAR applications, complementing the low-Q designs of conventional grating couplers.

5. PERFECT ABSORPTION WITH SINGLE-SIDED ILLUMINATION AND NO BACKING MIRRORS

We now discuss achieving perfect absorption in photonic crystal structures by combining the highly asymmetric coupling to different channels and matched radiative and nonradiative quality factors. Previous work on achieving perfect absorption has utilized metamaterial responses [19–21], interference between multiple incident directions [23–25], or a backing mirror to confine and trap light [26–32]. On the other hand, our results on achieving highly directional coupling suggest that it may be possible to achieve near-perfect absorption with single-sided illumination from the direction with strong coupling by only using dielectric structures and without the need for any backing mirrors. Intuitively, since the radiation coupling to one of the emission channels is strongly suppressed, there is only one direction to which the excited resonance can radiatively decay into. Appropriate tuning of the quality factor can then result in destructive interference toward this direction, thus achieving perfect absorption of the incident waves.

To incorporate material loss in our description, we include a nonradiative decay channel, setting τ_{nr} to be finite in Eq. (1). We assume that the loss rate is small and that the direct transmission pathway is not affected by the loss [28]. We start from a P-symmetric structure and incident direction where the coupling rates have a large asymmetry ratio. The parameters are chosen such that t is close to 1 and the asymmetry ratio saturates the bound $|d_2|/|d_1| = \sqrt{(1+t)/(1-t)}$. As shown in Supplement 1, P-symmetry and the time-reversal constraints Eqs. (4) and (5) imply that $d_1 = d_4 = \sqrt{(1-t)/\tau}\exp(-3\pi j/4)$, $d_2 = d_3 = \sqrt{(1+t)/\tau}\exp(-\pi j/4)$. Plugging this into the expressions for the power transmission and reflection coefficients, we find that on resonance $\omega = \omega_0$ and at critical coupling $\tau = \tau_{nr}$,

$$R_{14} = R_{23} = \frac{r^2}{4}, \qquad T_{14} = \left(\frac{1+t}{2}\right)^2, \qquad T_{23} = \left(\frac{1-t}{2}\right)^2, \tag{12}$$

$$A_{14} = 1 - R_{14} - T_{14} = \frac{1-t}{2}, \qquad A_{23} = \frac{1+t}{2}. \tag{13}$$

In the limit where $t \to 1$ and $r \to 0$, it follows that light incident from port 1 or 4 will be completely transmitted ($T_{14} = 1$), while light incident from port 2 or 3 will be completely absorbed ($A_{23} = 1 - R_{23} - T_{23} = 1$). A schematic of the resulting transmission and absorption characteristics is shown in Fig. 4(a).

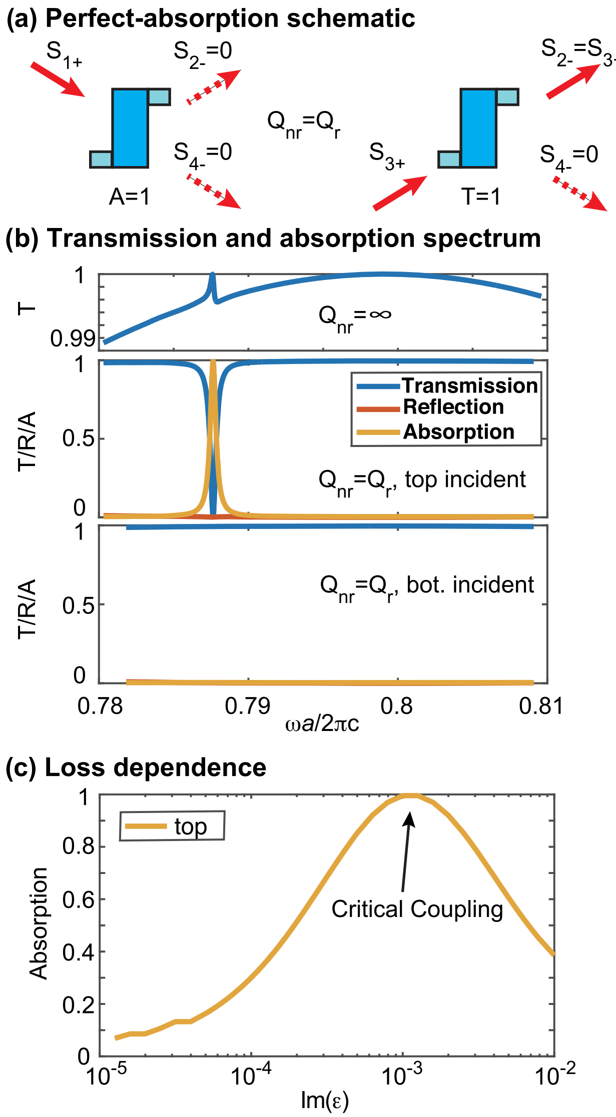

Fig. 4. Perfect absorption with single-sided illumination and no backing mirror for single-pass absorption less than 0.5%. (a) Schematic for perfect absorption at one incident angle and perfect transmission at the opposite incident angle. (b) Transmission, reflection, and absorption spectra for no loss ($Q_{nr} = \infty$) and critical loss ($Q_{nr} = Q_r$), consistent with the theoretical results in (a). (c) Loss dependence of absorption, showing near-perfect absorption for critical coupling.

To verify these analytical results, we performed numerical simulations of the transmission and reflection spectrum with the rigorous coupled-wave analysis (RCWA) method using a freely available software package [49]. The structural parameters are identical to the simulation in Fig. 3(a), with the difference being the addition of loss in the system. There is a slight shift of the resonance location relative to the Fabry–Perot background due to the different discretization schemes used in the FDTD and RCWA methods. Figure 4 shows the simulation results. As shown in Fig. 4(b), when no loss is present (top panel), the transmissivity is close to 1 in the vicinity of the resonance, reaching full transmission $T = 1$ at a single point on the Fano resonance as required by P-symmetry of the structure (see end of Section 2 for a discussion), and the reflectance is close to 0. With the addition of loss and with waves incident from the port with stronger coupling (incident direction is $\theta = 3.5°$ from normal, middle panel), the transmittance is reduced, and at critical coupling, the transmittance drops to 0 for the resonance frequency, resulting in the full absorption of the incoming waves. On the other hand, for the same lossy structure and for the opposite incident direction (bottom panel), there is negligible absorption and most of the waves are transmitted. In Fig. 4(c), we show the maximum absorption for a given incident angle as a function of loss, clearly showing a peak of near-perfect absorption at critical coupling. For other incident angles near that of maximum absorption, the Q-matching condition and asymmetric radiation condition are still approximately satisfied, giving rise to high absorption, and the absorption peak will shift to different frequencies following the band dispersion, as shown in Supplement 1, Fig. S5. Numerically, we find that when light is incident from the port with stronger coupling, the absorption can be as high as $A_{23} = 99.8\%$; when light is incident from the port with weaker coupling, the transmission is $T_{14} = 99.4\%$, while absorption is only $A_{14} = 0.5\%$ (this is roughly equal to the single-pass absorption rate of 0.4% in our simulations). The numerical simulations show excellent agreement with our TCMT predictions for a background Fabry–Perot transmissivity of $t = 0.996$ [Fig. 4(b)]; the small difference comes from the contribution of absorption to the Fabry–Perot background. Further numerical optimization placing the resonance frequency closer to the frequency of full transmission on the Fabry–Perot background could further increase on-resonance absorption in the desired port.

These results are widely applicable to many different absorbing materials. The wide range of achievable resonance quality factors, as discussed in the preceding section, implies that for both strong and weak absorbers, structures can be designed such that there is highly asymmetric coupling and critical coupling, yielding perfect absorption in the system. While our simulations were performed assuming a material with a spatially uniform absorption profile, the generality of the TCMT formalism ensures that it is also applicable to scenarios with only a thin active layer with absorption, such as with 2D materials [28,31,50].

6. DISCUSSION AND CONCLUSION

In conclusion, we developed a temporal coupled-mode theory formalism for general dielectric photonic crystal slab structures with arbitrary in-plane wavevectors, adequately taking into account the time-reversal-symmetry-related pair of resonances and coupling channels. Using this formalism, we derived general bounds on the asymmetric radiation rates to the top and bottom of a photonic crystal slab. We then used the intuitions developed from these bounds to show examples of highly asymmetric radiation from inversion-symmetric photonic crystal slabs, demonstrating strong asymmetry, rapid tuning, and a variety of quality factors for different applications. Moreover, we showed how the highly asymmetric coupling to the top and bottom of photonic crystal slabs can be used to achieve perfect absorption for light incident from a single side, for a single-pass absorption rate of less than 0.5%, without the need for a back-reflection mirror as in conventional setups. The highly directional radiation could greatly benefit applications such as PCSELs, grating couplers, and LIDARs, while achieving perfect absorption without the need for back-reflection mirrors could increase the efficiency and simplify the design of photodetectors and solar cells.

While our numerical examples focused on a particular structural design, the general principle of breaking C_2^z symmetry is applicable to a wide range of structures. We now briefly discuss how to implement such structures using readily available fabrication techniques. For example, gratings with slanted walls share the same structural symmetries as those in Fig. 2(a) and thus can approach perfect single-sided radiation and absorption as well. Such gratings can be fabricated using focused ion beam milling [51], angled etching with Faraday cages [52], or inclined lithography [53]. More generally, almost any of the techniques for fabricating blazed gratings [54,55] or constructing 3D photonic crystals [39] (e.g., layer-by-layer lithography or holographic lithography) could also be employed in a simplified form to make an asymmetric coating. A wide range of structures breaking C_2^z symmetry and achieving high asymmetry can thus be realized with these different techniques.

Our work provides new design principles for achieving highly directional radiation and perfect absorption in photonics and could be extended to systems where there are nonlinearities, gain and loss, different substrates and superstrates, and nonreciprocal structures with magneto-optical effects [56]. Our work can also be generalized to other systems characterized by temporal coupled-mode theory, such as in-plane chiral meta-surfaces, asymmetric ring resonators, and scattering from nano-plasmonic structures.

Funding. U.S. Army (W911NF-13-D0001); U.S. Department of Energy (DOE), Office of Science (SC) (DE-SC0001299); United States-Israel Binational Science Foundation (2013508); National Science Foundation (NSF) (DMR-1307632).

Acknowledgment. We thank Yong Liang, Ling Lu, Scott Skirlo, Yichen Shen, Emma Regan, Aviram Massuda, Francisco Machado, and Nicholas Rivera for the helpful discussions.

See Supplement 1 for supporting content.

REFERENCES

1. J. Lee, B. Zhen, S.-L. Chua, W. Qiu, J. D. Joannopoulos, M. Soljačić, and O. Shapira, "Observation and differentiation of unique high-Q optical resonances near zero wave vector in macroscopic photonic crystal slabs," Phys. Rev. Lett. **109**, 067401 (2012).
2. S. G. Johnson, S. Fan, P. R. Villeneuve, J. D. Joannopoulos, and L. A. Kolodziejski, "Guided modes in photonic crystal slabs," Phys. Rev. B **60**, 5751–5758 (1999).
3. S. Fan and J. D. Joannopoulos, "Analysis of guided resonances in photonic crystal slabs," Phys. Rev. B **65**, 235112 (2002).
4. W. Zhou, D. Zhao, Y.-C. Shuai, H. Yang, S. Chuwongin, A. Chadha, J.-H. Seo, K. X. Wang, V. Liu, Z. Ma, and S. Fan, "Progress in 2D photonic crystal Fano resonance photonics," Prog. Quantum Electron. **38**, 1–74 (2014).
5. W. Suh and S. Fan, "All-pass transmission or flattop reflection filters using a single photonic crystal slab," Appl. Phys. Lett. **84**, 4905 (2004).
6. K. Hirose, Y. Liang, Y. Kurosaka, A. Watanabe, T. Sugiyama, and S. Noda, "Watt-class high-power, high-beam-quality photonic-crystal lasers," Nat. Photonics **8**, 406–411 (2014).
7. E. Chow, A. Grot, L. W. Mirkarimi, M. Sigalas, and G. Girolami, "Ultracompact biochemical sensor built with two-dimensional photonic crystal microcavity," Opt. Lett. **29**, 1093–1095 (2004).
8. D. Taillaert, P. Bienstman, and R. Baets, "Compact efficient broadband grating coupler for silicon-on-insulator waveguides," Opt. Lett. **29**, 2749–2751 (2004).
9. R. L. Roncone, L. Li, K. A. Bates, J. J. Burke, L. Weisenbach, and B. J. Zelinski, "Design and fabrication of a single leakage-channel grating coupler," Appl. Opt. **32**, 4522–4528 (1993).
10. D. Vermeulen, S. Selvaraja, P. Verheyen, G. Lepage, W. Bogaerts, P. Absil, D. Van Thourhout, and G. Roelkens, "High-efficiency fiber-to-chip grating couplers realized using an advanced CMOS-compatible silicon-on-insulator platform," Opt. Express **18**, 18278–18283 (2010).
11. H. Subbaraman, X. Xu, A. Hosseini, X. Zhang, Y. Zhang, D. Kwong, and R. T. Chen, "Recent advances in silicon-based passive and active optical interconnects," Opt. Express **23**, 2487–2511 (2015).
12. M. Fan, M. Popović, and F. X. Kartner, "High directivity, vertical fiber-to-chip coupler with anisotropically radiating grating teeth," in *Conference on Lasers and Electro-Optics (CLEO)* (2007), paper CTuDD3.
13. Y. Ota, S. Iwamoto, and Y. Arakawa, "Asymmetric out-of-plane power distribution in a two-dimensional photonic crystal nanocavity," Opt. Lett. **40**, 3372–3375 (2015).
14. M. Liu, X. Yin, E. Ulin-Avila, B. Geng, T. Zentgraf, L. Ju, F. Wang, and X. Zhang, "A graphene-based broadband optical modulator," Nature **474**, 64–67 (2011).
15. F. Xia, T. Mueller, Y.-M. Lin, A. Valdes-Garcia, and P. Avouris, "Ultrafast graphene photodetector," Nat. Nanotechnol. **4**, 839–843 (2009).
16. Z. Yu, A. Raman, and S. Fan, "Fundamental limit of nanophotonic light trapping in solar cells," Proc. Natl. Acad. Sci. USA **107**, 17491–17496 (2010).
17. A. Pospischil, M. M. Furchi, and T. Mueller, "Solar-energy conversion and light emission in an atomic monolayer p-n diode," Nat. Nanotechnol. **9**, 257–261 (2014).
18. L. N. Hadley and D. M. Dennison, "Reflection and transmission interference filters part I theory," J. Opt. Soc. Am. **37**, 451–465 (1947).
19. Y. Ra'di, V. S. Asadchy, and S. A. Tretyakov, "Total absorption of electromagnetic waves in ultimately thin layers," IEEE Trans. Antennas Propag. **61**, 4606–4614 (2013).
20. N. I. Landy, S. Sajuyigbe, J. J. Mock, D. R. Smith, and W. J. Padilla, "Perfect metamaterial absorber," Phys. Rev. Lett. **100**, 207402 (2008).
21. C. M. Watts, X. Liu, and W. J. Padilla, "Metamaterial electromagnetic wave absorbers," Adv. Mater. **24**, OP98–OP120 (2012).
22. D. G. Baranov, J. H. Edgar, T. Hoffman, N. Bassim, and J. D. Caldwell, "Perfect interferenceless absorption at infrared frequencies by a vander Waals crystal," Phys. Rev. B **92**, 201405 (2015).
23. Y. D. Chong, L. Ge, H. Cao, and A. D. Stone, "Coherent perfect absorbers: time-reversed lasers," Phys. Rev. Lett. **105**, 053901 (2010).
24. W. Wan, Y. D. Chong, L. Ge, H. Noh, A. D. Stone, and H. Cao, "Time-reversed lasing and interferometric control of absorption," Science **331**, 889–892 (2011).
25. Y. Sun, W. Tan, H.-Q. Li, J. Li, and H. Chen, "Experimental demonstration of a coherent perfect absorber with PT phase transition," Phys. Rev. Lett. **112**, 143903 (2014).
26. J. R. Tischler, M. S. Bradley, and V. Bulović, "Critically coupled resonators in vertical geometry using a planar mirror and a 5 nm thick absorbing film," Opt. Lett. **31**, 2045 (2006).
27. C.-H. Lin, R.-L. Chern, and H.-Y. Lin, "Polarization-independent broad-band nearly perfect absorbers in the visible regime," Opt. Express **19**, 415–424 (2011).
28. J. R. Piper and S. Fan, "Total absorption in a graphene monolayer in the optical regime by critical coupling with a photonic crystal guided resonance," ACS Photon. **1**, 347–353 (2014).
29. Y. Liu, A. Chadha, D. Zhao, J. R. Piper, Y. Jia, Y. Shuai, L. Menon, H. Yang, Z. Ma, S. Fan, F. Xia, and W. Zhou, "Approaching total absorption at near infrared in a large area monolayer graphene by critical coupling," Appl. Phys. Lett. **105**, 181105 (2014).
30. L. Zhu, F. Liu, H. Lin, J. Hu, Z. Yu, X. Wang, and S. Fan, "Angle-selective perfect absorption with two-dimensional materials," Light Sci. Appl. **5**, e16052 (2015).
31. J. R. Piper and S. Fan, "Broadband absorption enhancement in solar cells with an atomically thin active layer," ACS Photon. **3**, 571–577 (2016).
32. B. C. P. Sturmberg, T. K. Chong, D.-Y. Choi, T. P. White, L. C. Botten, K. B. Dossou, C. G. Poulton, K. R. Catchpole, R. C. McPhedran, and C. Martijn de Sterke, "Total absorption of visible light in ultrathin weakly absorbing semiconductor gratings," Optica **3**, 556–562 (2016).
33. V. Ganapati, O. D. Miller, and E. Yablonovitch, "Light trapping textures designed by electromagnetic optimization for subwavelength thick solar cells," IEEE J. Photovoltaics **4**, 175–182 (2014).
34. A. Oskooi, Y. Tanaka, and S. Noda, "Tandem photonic-crystal thin films surpassing Lambertian light-trapping limit over broad bandwidth and angular range," Appl. Phys. Lett. **104**, 091121 (2014).
35. J. R. Piper, V. Liu, and S. Fan, "Total absorption by degenerate critical coupling," Appl. Phys. Lett. **104**, 251110 (2014).

36. K. X. Wang, Z. Yu, S. Sandhu, and S. Fan, “Fundamental bounds on decay rates in asymmetric single-mode optical resonators,” Opt. Lett. **38**, 100–102 (2013).
37. W. Suh, Z. Wang, and S. Fan, “Temporal coupled-mode theory and the presence of non-orthogonal modes in lossless multimode cavities,” IEEE J. Quantum Electron. **40**, 1511–1518 (2004).
38. S. Fan, W. Suh, and J. D. Joannopoulos, “Temporal coupled-mode theory for the Fano resonance in optical resonators,” J. Opt. Soc. Am. A **20**, 569–572 (2003).
39. J. D. Joannopoulos, S. G. Johnson, J. N. Winn, and R. D. Meade, *Photonic Crystals: Molding the Flow of Light*, 2nd ed. (Princeton University, 2011).
40. C. W. Hsu, B. Zhen, S.-L. Chua, S. G. Johnson, J. D. Joannopoulos, and M. Soljačić, “Bloch surface eigenstates within the radiation continuum,” Light Sci. Appl. **2**, e84 (2013).
41. Z. Ruan and S. Fan, “Temporal coupled-mode theory for light scattering by an arbitrarily shaped object supporting a single resonance,” Phys. Rev. A **85**, 043828 (2012).
42. M. T. Wade, F. Pavanello, R. Kumar, C. M. Gentry, A. Atabaki, R. Ram, V. Stojanovic, and M. A. Popovic, “75% efficient wide bandwidth grating couplers in a 45 nm microelectronics CMOS process,” in *IEEE Optical Interconnects Conference (OI)* (IEEE, 2015), pp. 46–47.
43. A. Taflove, A. F. Oskooi, and S. G. Johnson, *Advances in FDTD Computational Electrodynamics: Photonics and Nanotechnology* (Artech House, 2013).
44. A. F. Oskooi, D. Roundy, M. Ibanescu, P. Bermel, J. D. Joannopoulos, and S. G. Johnson, “Meep: A flexible free-software package for electromagnetic simulations by the FDTD method,” Comput. Phys. Commun. **181**, 687–702 (2010).
45. A. Yaacobi, J. Sun, M. Moresco, G. Leake, D. Coolbaugh, and M. R. Watts, “Integrated phased array for wide-angle beam steering,” Opt. Lett. **39**, 4575–4578 (2014).
46. B. Zhen, C. W. Hsu, L. Lu, A. D. Stone, and M. Soljačić, “Topological nature of optical bound states in the continuum,” Phys. Rev. Lett. **113**, 257401 (2014).
47. C. W. Hsu, B. Zhen, J. Lee, S.-L. Chua, S. G. Johnson, J. D. Joannopoulos, and M. Soljačić, “Observation of trapped light within the radiation continuum,” Nature **499**, 188–191 (2013).
48. C. W. Hsu, B. Zhen, A. D. Stone, J. D. Joannopoulos, and M. Soljačić, “Bound states in the continuum,” Nat. Rev. Mater. **1**, 16048 (2016).
49. V. Liu and S. Fan, “S4: a free electromagnetic solver for layered periodic structures,” Comput. Phys. Commun. **183**, 2233–2244 (2012).
50. K. F. Mak, C. Lee, J. Hone, J. Shan, and T. F. Heinz, “Atomically thin MoS_2: a new direct-gap semiconductor,” Phys. Rev. Lett. **105**, 136805 (2010).
51. J. Schrauwen, F. V. Laere, D. V. Thourhout, and R. Baets, “Focused-ion-beam fabrication of slanted grating couplers in silicon-on-insulator waveguides,” IEEE Photon. Technol. Lett. **19**, 816–818 (2007).
52. M. J. Burek, N. P. de Leon, B. J. Shields, B. J. M. Hausmann, Y. Chu, Q. Quan, A. S. Zibrov, H. Park, M. D. Lukin, and M. Lončar, “Free-standing mechanical and photonic nanostructures in single-crystal diamond,” Nano Lett. **12**, 6084–6089 (2012).
53. A. del Campo and E. Arzt, “Fabrication approaches for generating complex micro- and nanopatterns on polymeric surfaces,” Chem. Rev. **108**, 911–945 (2008).
54. T. Fujita, H. Nishihara, and J. Koyama, “Blazed gratings and Fresnel lenses fabricated by electron-beam lithography,” Opt. Lett. **7**, 578–580 (1982).
55. C. A. Palmer and E. G. Loewen, *Diffraction Grating Handbook*, 6th ed. (Newport Corporation, 2005).
56. Z. Wang and S. Fan, “Magneto-optical defects in two-dimensional photonic crystals,” Appl. Phys. B **81**, 369–375 (2005).